Contents lists available at ScienceDirect

Mechatronics

journal homepage: www.elsevier.com/locate/mechatronics

An electrostatically suspended contactless platform ☆

Michael Andonian, Robert T. M'Closkey *

Mechanical and Aerospace Engineering Department, Samueli School of Engineering and Applied Science, University of California, Los Angeles, 420 Westwood Plaza, Los Angeles, CA 90095, United States of America

ARTICLE INFO

Keywords:
Electrostatic levitation
Electrostatic suspension
Differential capacitance sensor
Contact-free platform

ABSTRACT

Electrostatic suspension of a silicon disk with explicit control of the lateral translational degrees-of-freedom is reported. The transduction subsystem configures electrode pairs to exert electrostatic forces on the disk and to also measure differential capacitances related to the disk position. Disk sidewall forcing electrodes are not necessary to control the disk's lateral position because tilting the disk relative to the plane of the electrodes exerts lateral forces on the disk. Despite the fact that the disk's lateral and angular degrees-of-freedom are strongly coupled, the system is not strongly stabilizable using only the disk's vertical position and tilt estimates derived from electrode–disk gap measurements. Nevertheless, a stabilizing controller is proposed and lateral position measurements are added for regulating the disk's in-plane position. Extensive experimental results corroborate the model and analysis.

1. Introduction

This paper describes the fabrication, modeling, analysis, and testing of a system that electrostatically suspends a silicon disk situated between two sets of electrodes. The rigid body motion of the disk is controlled with the exception of yaw as this variable is not observable with the electrode arrangement. Electrostatically levitated structures in the context of suspended proof masses for sensors have been reported in [1–4], however, the spherical proof masses described in these references only require stabilization of three translational degrees-of-freedom. It is demonstrated in the present paper how the stabilization problem significantly differs for the disk since the three translational degrees-of-freedom are strongly coupled to the two tilt degrees-of-freedom. Furthermore, the system presented herein does not rely on fringe field forces to passively stabilize the lateral degrees-of-freedom.

Contactless manipulation of disks has been demonstrated in [5–7] for the purpose of handling storage media. The disks' lateral degrees-of-freedom were not explicitly modeled and in practice are passively stabilized by fringe-field electrostatic forces which tend to center the disk under the electrodes. In [8] it was reported how shifts in the resonant frequencies of LC circuits in which the capacitances are established by the electrode–plate gaps can be exploited to levitate a square plate. This approach has the advantage of requiring no explicit feedback control, however, like the prior references, it relies on passive centering of the plate's lateral translational degrees of freedom. The electrode dimensions for the system reported in this paper do not exert strong fringe-field forces on the disk and so the lateral degrees-of-freedom must be stabilized by the feedback controller. Including the lateral degrees-of-freedom in the analysis reveals strong coupling to the tilt, or angular, disk variables. From an analytical perspective, stabilization of the disk's vertical and angular variables also stabilizes its lateral variables, however, in practice, regulation of the disk's lateral position requires direct measurements of these quantities. This is clearly established in the analysis of the model and the experimental results. The lateral degrees-of-freedom of the suspended ring gyro reported in [9] are stabilized via in-plane electrodes. These electrodes constrain the permissible lateral motion of the ring, however, this was not a limitation for the proposed application.

One intended application of this research is a platform for studying the dynamics of micro-scale systems in which system-substrate contact has been eliminated. An example is the planar MEMS resonator reported in [10]. Suspension of the resonator would provide controllable and repeatable resonator boundary conditions. The transduction system described herein can scale to accommodate such resonators: a platform approximately 1 cm in diameter would require gaps of 2-3 μm to preserve the same electrode–disk capacitances (77 pF) as the system reported in this paper.

The transduction system is modeled after the approach used in the North American Aviation Electrostatically Levitated Gyro (ESG) [1,2]. This approach configures the electrodes with transformers in order to measure differential capacitances related to the disk position. The same

☆ This paper was recommended for publication by Associate Editor Jason J. Gorman.

* Corresponding author.
E-mail addresses: andonian23@g.ucla.edu (M. Andonian), rtm@seas.ucla.edu (R.T. M'Closkey).

https://doi.org/10.1016/j.mechatronics.2021.102685
Received 29 September 2020; Received in revised form 19 May 2021; Accepted 15 October 2021

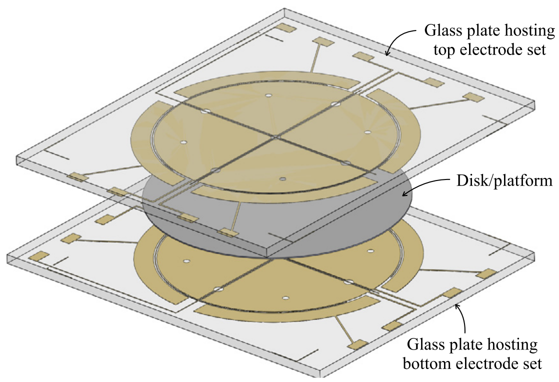

Fig. 1. View of the glass plates and electrodes for suspending the silicon disk. The disk is 8.2 cm in diameter. Spacers between the glass plates are used to set the electrode–disk gaps to be 134 μm when the disk is centered between, and parallel to, the electrode sets.

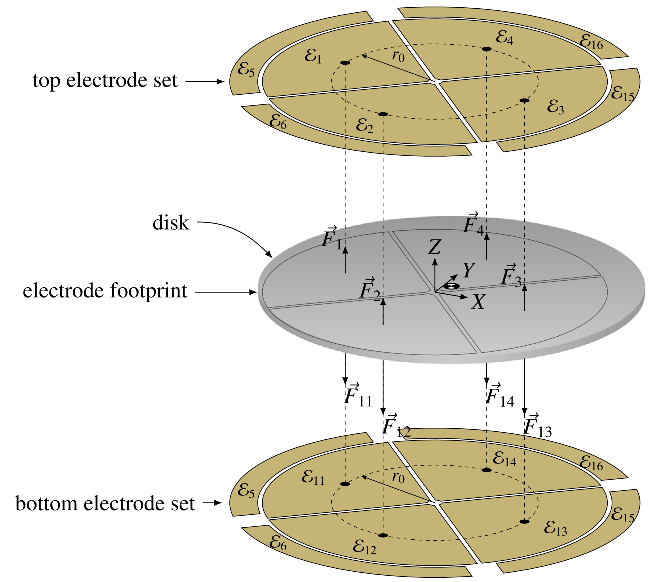

Fig. 2. View of the electrode configuration and disk. The *primary electrodes* are labeled $\mathcal{E}_1$, $\mathcal{E}_2$, $\mathcal{E}_3$ and $\mathcal{E}_4$ for the top electrode set, and $\mathcal{E}_{11}$, $\mathcal{E}_{12}$, $\mathcal{E}_{13}$ and $\mathcal{E}_{14}$ for the bottom electrode set. The *lateral electrodes* are labeled $\mathcal{E}_5$, $\mathcal{E}_{15}$, $\mathcal{E}_6$ and $\mathcal{E}_{16}$. Note that a single lateral electrode has an element on both the top and bottom. The disk center of mass is displaced from the inertial X-Y-Z frame.

electrodes are also used to exert the controlled electrostatic forces on the disk. By using a given pair of electrodes as both a capacitive pick-off and an electrostatic forcer, the measured capacitance is maximized and the voltages required for controlled suspension are minimized for a given electrode size. While this dual function of the electrodes reduces the complexity of the electronics and system design, considerable "feedthrough" is produced from the control signal to measurements of the electrode–disk gaps. This feedthrough must be removed from the measurements prior to implementing the controllers. Compensation in the ESG was achieved with a parallel "model transformer" –essentially an analog feedforward filter based on using matched transformers with fixed capacitances representing the electrode-proof mass capacitance when the proof mass is centered. In the present paper, a filter implemented in the DSP achieves the desired cancellation of the feedthrough. The modeling paradigm for the transduction and the feedforward compensation approaches were developed in [11,12] and are extended to the system presented in this paper.

The paper is organized as follows: Section 2 describes the geometry and electrical interface of the electrode–disk system; Section 3 briefly discusses fabrication; Section 4 develops and analyzes the system model; Section 5 addresses controller design; Section 6 presents the experimental results and validates the modeling paradigm; Section 7 concludes the paper.

2. System description

2.1. Electrode and disk geometry

The electrode–disk arrangement is shown in Fig. 1. The silicon disk diameter is 8.2 cm and its thickness is 400 μm. The electrode patterns on the top and bottom glass plates are identical. The plates are assembled so that they are parallel and an electrode on the top plate is aligned with a mirror-image electrode on the bottom plate. When the disk is uniformly centered between the sets of electrodes there is an electrode–disk gap of approximately 134 μm between the top of the disk and top electrode set, and a 134 μm gap between the bottom of the disk and the bottom electrode set. Additional details are given in the Appendix. The schematic in Fig. 2 identifies the electrodes and shows an exploded view of the assembly (the electrode–disk gaps are not to scale). The four pie-shaped *primary electrodes* are labeled $\mathcal{E}_1$ through $\mathcal{E}_4$ for the top set and $\mathcal{E}_{11}$ through $\mathcal{E}_{14}$ for the bottom set. The primary electrodes are grouped into four pairs: the electrodes immediately facing each other (with the disk between them) form one pair, e.g., $\mathcal{E}_1$ and $\mathcal{E}_{11}$ form one primary pair. The primary pairs exert controlled electrostatic forces on the disk and also measure differential electrode–disk capacitances. The capacitance measurements are related to the electrode–disk gaps associated with each primary pair and can be used to directly estimate the disk's center of mass vertical position and the two tilt angles (the disk is treated as a rigid body). It will be shown that the primary electrodes can stabilize the rigid body motion of the disk with the exception of "yaw" motion about the Z axis. Yaw is not observable using these measurements and so is not controlled.

Lateral motion in the X-Y plane is also stabilized using only the primary electrodes because the lateral and tilt degrees-of-freedom are coupled in the suspended disk. It is possible, in principle, to control the lateral position of the disk without lateral measurements, however, effective regulation requires direct measurement of these quantities. To wit, the disk's position in the X-Y plane is measured with *lateral electrodes*. In reality there are only four lateral electrodes because mirror image electrodes on the top and bottom plates actually form a single electrode as suggested by the labels in Fig. 2. The lateral electrodes are also grouped into (two) pairs with antipodal electrodes creating a pair, e.g., $\mathcal{E}_5$ and $\mathcal{E}_{15}$ form a lateral pair, and $\mathcal{E}_6$ and $\mathcal{E}_{16}$ form the second pair. A lateral pair provides a differential capacitance measurement proportional to the lateral position of the disk relative to the pair, e.g., $\mathcal{E}_5$ and $\mathcal{E}_{15}$ measure disk displacement in the X coordinate direction. The lateral electrode configuration also largely rejects the disk's vertical and tilting rigid body motion.

The differential capacitance measurements provide convenient *null* positions: if all differential capacitances of the primary pairs are zero then the disk is parallel to the electrodes with uniform and equal gaps between the disk and primary electrodes (this assumes an ideal transformer model with no parasitic capacitance; in practice, there exist measurement offsets, but these are easily removed). Similarly, if the differential capacitances of the lateral pairs are zero then the disk is symmetrically centered relative to the lateral electrodes. Deviation from the null positions generate non-zero measurements that are acted upon by the controller.

The diameter spanned by the primary electrodes is smaller than the disk diameter and consequently when the disk is near its null position the in-plane forces exerted on the disk by the primary electrodes' electrical fringe fields are, in a practical sense, zero. The lateral electrodes are operated at lower potentials and their fringe field forces are not modeled. It is possible to exert in-plane forces on the disk, however, this requires that the disk be tilted relative to the plane of the electrodes: the disk is an equipotential body so the field lines are normal to the disk's top and bottom surface; if the disk is titled to be non-parallel to the primary electrodes, the electrostatic forces exerted on the disk will have a non-zero in-plane component. It will be shown how this property can be exploited to control the disk's lateral position.

2.2. Interface to electrodes

The pairing of primary electrodes is achieved with transformers as illustrated in Fig. 3. A given primary pair is connected to its transformer's primary leads. The transformer's primary windings have equal inductances connected at the center tap (ct). The center tap is driven with a sinusoidal current

$$i_{\mathrm{ct}}(t) = a_{\mathrm{ct}} \cos\left(\omega_0 t\right),$$

where a_{ct} is the (constant) amplitude and ω_0 is the carrier frequency. An auxiliary transformer is connected to the center taps of two transformers linked to two primary electrode pairs. In this configuration, current flowing onto the disk through one center tap is pulled off through the "adjacent" center tap as indicated in Fig. 3. Thus, if the disk is initially at ground potential, it is maintained at ground potential even when suspended. By maintaining the disk at ground, any difference between the capacitances in a pair of primary electrodes will produce a sinusoidal voltage drop across the transformer's secondary windings. For example, the primary pairs $\mathcal{E}_k$ and $\mathcal{E}_{1k}$, $k = 1, 2, 3, 4$, are associated with capacitances C_k and C_{1k}; if $C_k = C_{1k}$, indicating that the average gap between the disk and $\mathcal{E}_k$ is equal to the average gap between the disk and $\mathcal{E}_{1k}$, then $v_{\mathrm{s},k} = 0$, where $v_{\mathrm{s},k}$ is the "sense voltage" across the secondary winding associated with the kth set of paired electrodes. On the other hand, if the average gaps are not equal ($C_k \neq C_{1k}$) then $v_{\mathrm{s},k}$ is sinusoidal with frequency ω_0. Synchronous demodulation of $v_{\mathrm{s},k}$ yields a signal proportional to the imbalance in the electrode–disk gap associated with $\mathcal{E}_k$ and $\mathcal{E}_{1k}$. The phase of the demodulator is chosen to maximize the component of $v_{\mathrm{s},k}$ due to disk displacement from its null position. The center tap current provides the master phase against which all sinusoidal signals are referenced. Furthermore, the inductances of the transformer primary windings are large enough such that the nominal inductor–capacitor resonant frequency is less than the carrier frequency so, to first order, the center tap current is evenly split between the primary inductances in a given transformer independent of the electrode–disk capacitances. This effectively controls the charge on the electrodes and softens the pull-in due to the electrostatic forces because as an electrode–disk gap is decreased, the voltage potential between them is also decreased. More details on controlling charge in a parallel-plate actuator is discussed in [13].

The transformers are also used for exerting controlled electrostatic forces on the disk. The "control potential" $v_{\mathrm{c},k}(t) = a_{\mathrm{c},k}(t)\cos(\omega_0 t + \phi_{c,k})$ is applied at resistor R_{c} that is in series with the transformer secondary load as shown in Fig. 3. This produces a differential sinusoidal potential on each electrode in a primary electrode pair, i.e., electrode potentials arising from $v_{\mathrm{c},k}$ invariably have a 180° phase difference due to the magnetic coupling within the transformer windings. In contrast, the i_{ct}-induced potentials on both electrodes are in-phase with one another. The superposed effects of i_{ct} and $v_{\mathrm{c},k}$ are sinusoidal with frequency ω_0 and so the control signal phase $\phi_{\mathrm{c},k}$ is selected so the $v_{\mathrm{c},k}$-induced component on electrode $\mathcal{E}_k$ is in-phase with the i_{ct}-induced voltage and therefore the $v_{\mathrm{c},k}$-induced component of $\mathcal{E}_{1k}$ is 180° out of phase with the i_{ct}-induced component. When $\phi_{\mathrm{c},k}$ is chosen in this manner, changing $a_{\mathrm{c},k}$ produces a *differential* change in the *amplitudes* of the sinusoidal potentials on the paired electrodes while maintaining the disk at ground potential. This creates the largest differential electrostatic force on the disk for a given value of $a_{\mathrm{c},k}$ because the electrostatic forces are proportional to the square of the electrode voltages. In fact, as far as the disk is concerned, the mean square value of the electrode voltages

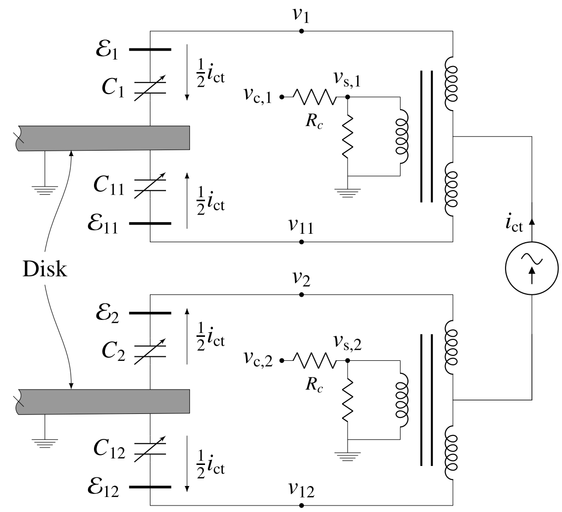

Fig. 3. Circuit schematic illustrating the connection between the transformers and the $\mathcal{E}_1$-$\mathcal{E}_{11}$ and $\mathcal{E}_2$-$\mathcal{E}_{12}$ pairs of primary electrodes. The corresponding capacitances developed between the electrodes and disk are also shown. The disk is not physically grounded, however, the notation is used to convey that the disk is at ground potential due to the coordination of the center tap currents. The connection to $\mathcal{E}_3$-$\mathcal{E}_{13}$ and $\mathcal{E}_4$-$\mathcal{E}_{14}$ is identical.

over a certain bandwidth creates "effective" forces can be used as a proxies for the exact electrostatic forces because the disk acts as a low-pass filter. This fact is exploited in deriving the linear, time-invariant discrete-time model of the system described in Section 4.4.

The amplitude-modulated sinusoids $v_{\mathrm{s},k}$ and $v_{\mathrm{c},k}$ are related to baseband signals that are sampled and manipulated by the discrete-time controller. The modulation/demodulation shown in Fig. 4 is accomplished with analog electronics. A DSP implements the feedforward filters, coordinate transformations, and feedback compensation. The "baseband" signals $\{u_1, u_2, u_3, u_4\}$ (input) and $\{\zeta_1, \zeta_2, \zeta_3, \zeta_4\}$ (output) represent an electro-mechanical model of the suspended disk.

The lateral electrodes, $\mathcal{E}_5$, $\mathcal{E}_{15}$, $\mathcal{E}_6$, and $\mathcal{E}_{16}$, measure lateral displacements of the disk and are connected to transformers according to Fig. 5. In this configuration, lateral translations of the disk change the overlapping areas between the disk and the paired lateral electrodes. The voltage drop across the transformer secondary is proportional to differential capacitance arising from the differential area change. These electrodes are not biased by a control voltage and therefore their potentials are dictated by the potential established by the center tap current and lateral electrode–disk capacitances. Although the same symbol is used to denote the center tap current for the lateral electrodes it is typically 10% of the current supplied to the primary electrodes. The lateral electrodes provide the additional baseband measurements $\{\zeta_5, \zeta_6\}$.

3. Electrode and disk fabrication

Two 3 mm thick glass substrates are patterned to produce the electrodes and wirebond pads. These patterns consist of a metal stack of Ti, Ag, and Au, with thicknesses of 10 nm, 2 μm, and 200 nm, respectively. The wire bond pads are used to connect the transformer leads to the electrodes. To protect the electrodes and disk from voltage breakdown, a 20 μm layer of photoresist is hard baked on top of the exposed electrodes. This protective layer significantly increases the dielectric strength between the disk and electrodes and also ensures the disk never comes in contact with the electrodes. The disk is etched out of a 400 μm thick, double-side polished silicon wafer. A layer of aluminum is sputtered onto the disk to create an electrically conductive body so that the disk can be modeled as an equipotential body. The desired electrode–disk gaps are created with precision spacers. Alignment markers on both glass plates assist with the assembly. The relevant dimensions are given in the Appendix.

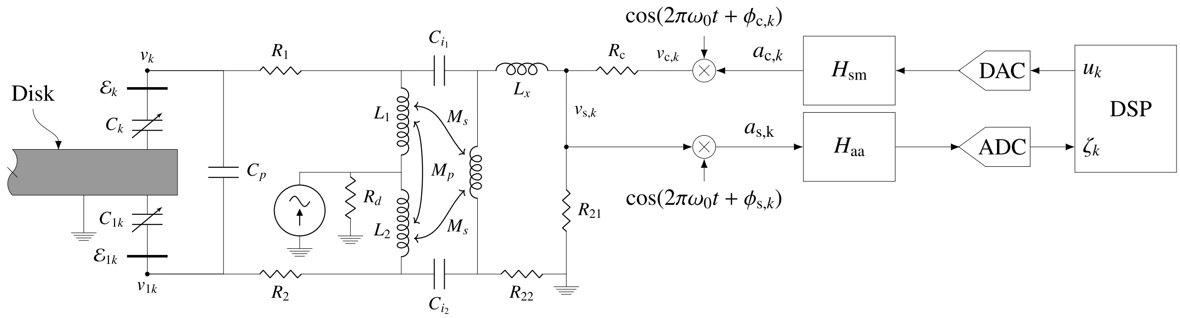

Fig. 4. Interface between the DSP and transformer signals for the primary electrodes. The anti-alias and smoothing filters are denoted H_{aa} and H_{sm}, respectively. The lateral electrodes use a similar demodulation scheme, however, since no control signals are associated with the lateral electrodes, the modulation path is not present for the lateral electrode signal conditioning.

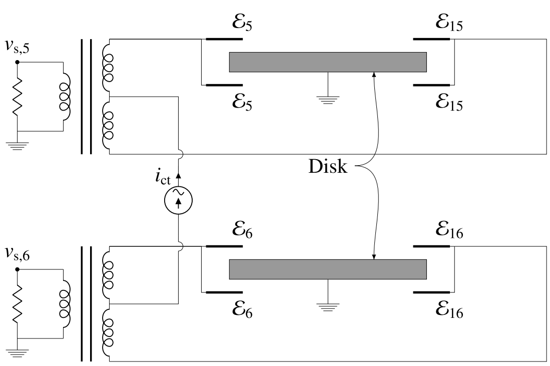

Fig. 5. Pairing of lateral electrodes for sensing the position of the disk in the X-Y plane. Note $\mathcal{E}_5$ is antipodal to $\mathcal{E}_{15}$, and $\mathcal{E}_6$ is antipodal to $\mathcal{E}_{16}$, as shown in Fig. 2.

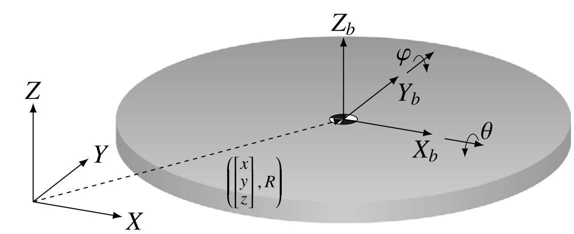

Fig. 6. The kinematic variables used to define the disk position relative the inertial XYZ-frame. Translations of the disk centroid relative to the XYZ-frame are denoted by $\{x, y, z\}$ while the rotation matrix R specifies the orientation of the disk-fixed $X_bY_bZ_b$-frame using Euler angles θ and φ.

4. Model

The suspended disk dynamics and the circuit equations are coupled by the electrode–disk capacitances and corresponding electrostatic forces. The following are assumed in deriving the equations of motion:

1. The electrostatic forces exerted on the disk by the lateral electrodes are neglected. These electrodes are significantly smaller than the primary electrodes and are operated at lower potentials.
2. The disk is assumed to be *thin* so calculation of electrode–disk gaps is determined by the deflection of disk center plane. Small angle approximations are used for defining the gaps.
3. The electrode–disk capacitances are defined using a simple parallel plate model in which the plate separation is taken to be the electrode–disk distance measured normally from the centroid of the electrode to the disk surface.
4. The electrostatic forces exerted on the plate are computed using the same parallel plate model as the capacitances.
5. Small-angle approximations are used when deriving the force components in the inertial frame and the moment expressions for the body-fixed frame.

These assumptions are quite reasonable since the disk is constrained to very small rotations and its diameter-to-thickness ratio is approximately 100. The equations of motion for the disk and electrical subsystem are derived in Sections 4.1 and 4.2. The model is linearized about an equilibrium point for the disk and yields a linear, time-periodic model in Section 4.3. An approximation technique is proposed in Section 4.4 that produces a linear, time-invariant discrete-time model that is used for system analysis and control design.

4.1. Disk equations

The disk kinematics are parameterized by $\{x, y, z\}$ and the Euler angles $\{\varphi, \theta\}$ (Fig. 6). Yaw motion is ignored and it is assumed that no gyroscopic forces are present. The origin of the X-Y-Z inertial reference frame is fixed at the centroid of the electrode sets. The disk's body-fixed frame, X_b-Y_b-Z_b, has its origin at the disk center of mass and is defined to be coincident with the inertial frame when the disk is in its *equilibrium configuration* (the values of the generalized coordinates are equal zero). Translations of the disk centroid along the principal axes X, Y, and Z are denoted by x, y, and z, respectively, while the successive rotations about the X_b-axis and Y_b-axis are given by the θ-φ Euler angle sequence. The body-fixed axes X_b and Y_b remain in the disk plane. To compute capacitances and electrostatic forces, electrode–disk gaps must be defined. The *change* in an electrode–disk gap when the disk is not in its equilibrium configuration is determined by computing the Z-displacement of the disk plane (defined by the X_b-Y_b plane) from the X-Y plane along the line through the centroids of paired electrodes — see Fig. 7. A positive change in gap is defined when the electrode centroid projected onto the X_b-Y_b plane is displaced in a positive Z sense relative to the X-Y plane. There is only one gap change defined for a given set of paired electrodes. The change in gaps are given by

$$\begin{aligned} z_1 &= z + \left(r_0 + x\right)\varphi - y\theta \\ z_2 &= z - \left(r_0 + y\right)\theta + x\varphi \\ z_3 &= z - \left(r_0 - x\right)\varphi - y\theta \\ z_4 &= z + \left(r_0 - y\right)\theta + x\varphi. \end{aligned} \tag{1}$$

where r_0 represents the radius of a circle in the electrode plane that interpolates the primary electrodes' centroids. Thus, the $\mathcal{E}_1$-disk gap is given by $z_0 - z_1$, the $\mathcal{E}_{11}$-disk gap is given by $z_0 + z_1$, the $\mathcal{E}_2$-disk gap is given by $z_0 - z_2$, and so forth. Similarly, the electrostatic forces are replaced with point forces denoted $\left\{\vec{F}_1, \ldots, \vec{F}_4\right\}$ for the top electrode set and $\left\{\vec{F}_{11}, \ldots, \vec{F}_{14}\right\}$ for the bottom electrode set (refer to Figs. 2 and 7). The magnitude of these forces are indicated in the same

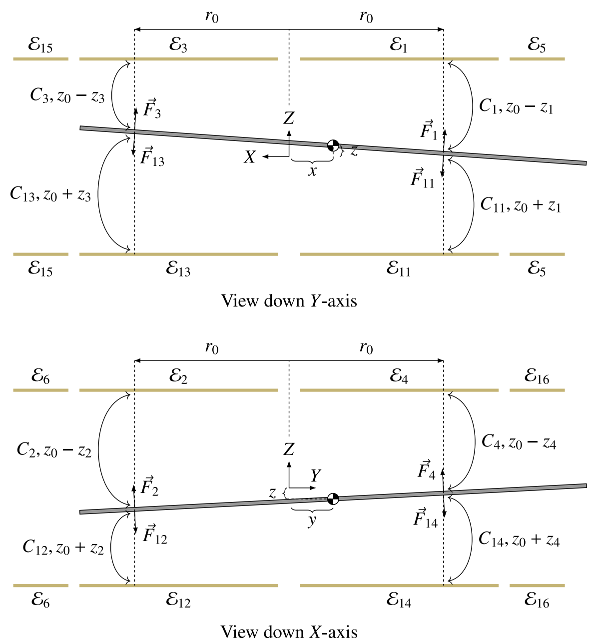

Fig. 7. Side views of the disk in relation to the electrode configuration (not to scale). The disk is assumed to be thin for the purpose of determining the locations of the electrostatic forces acting on it.

manner, however, the vector notation is dropped, e.g., F_1 represents the magnitude of $\vec{F}_1$. Despite the fact that a parallel plate model is used to determine the magnitude of the electrostatic forces, the point forces act normal to disk surface since the disk is assumed to be an equipotential body. Thus, when the X_b-Y_b is not coplanar with X-Y, forces in the X and Y directions are developed from the electrostatic forces. The electrostatic forces from the lateral electrodes are not modeled. The capacitances are determined from a parallel plate model using the effective electrode–disk gaps

$$C_k(q) = \frac{\epsilon_0 \epsilon_r A_\mathrm{p}}{z_0 - z_k} \quad k = 1, \ldots, 4, \tag{2}$$

$$C_{1k}(q) = \frac{\epsilon_0 \epsilon_r A_\mathrm{p}}{z_0 + z_k} \quad k = 1, \ldots, 4. \tag{3}$$

where A_p represents the primary electrode area. The area is fixed since it is assumed the disk is always interposed between the electrodes, i.e. the electrodes in a primary pair are never exposed to each other. In the disk's equilibrium configuration, zero differential capacitance is measured by the transformer secondary voltage drop because $C_k(0) = C_{1k}(0)$.

The magnitudes of the electrostatic forces associated with a given primary electrode pair $\mathcal{E}_k$ and $\mathcal{E}_{1k}$ are similarly computed assuming a parallel plate model,

$$\begin{aligned} F_k &= \frac{\epsilon_0 \epsilon_r A_\mathrm{p}}{2(z_0 - z_k)^2} v_k^2 \\ F_{1k} &= \frac{\epsilon_0 \epsilon_r A_\mathrm{p}}{2(z_0 + z_k)^2} v_{1k}^2. \end{aligned} \tag{4}$$

Lagrange's method yields the disk equations of motion,

$$\begin{aligned} & m\ddot{x} = Q_x \\ & m\ddot{y} = Q_y \\ & m\ddot{z} + mg = Q_z - c_z \dot{z} \\ & (J_{xy}\cos^2\varphi + J_z \sin^2\varphi)\ddot{\theta} + \dot{\varphi}\sin(2\varphi)(J_z - J_{xy})\dot{\theta} = Q_\theta - c_\theta \dot{\theta} \\ & J_{xy}\ddot{\varphi} + \frac{1}{2}\sin(2\varphi)(J_{xy} - J_z)\dot{\theta}^2 = Q_\varphi - c_\varphi \dot{\varphi} \end{aligned} \tag{5}$$

where m and $\{J_z, J_{xy}\}$ represent the disk mass and moments of inertia, respectively. The terms c_z, c_θ, and c_φ represent squeeze-film damping between the disk and the electrodes. The damping estimates are taken from [14]. The generalized forces associated with the generalized coordinates are computed assuming small angles. The details of these routine calculations are not given, however, they yield,

$$\begin{aligned} Q_x &= \varphi \sum_{k=1}^{4} F_k - F_{1k} \\ Q_y &= -\theta \sum_{k=1}^{4} F_k - F_{1k} \\ Q_z &= \sum_{k=1}^{4} F_k - F_{1k} \\ Q_\theta &= -(r_0 + y)(F_2 - F_{12}) + (r_0 - y)(F_3 - F_{13}) - y \sum_{k=1,3} F_k - F_{1k} \\ Q_\varphi &= (r_0 + x)(F_1 - F_{11}) - (r_0 - x)(F_3 - F_{13}) + x \sum_{k=2,4} F_k - F_{1k} \end{aligned}$$

A distinctive feature of these equations is the fact that forces in the *lateral* directions are only produced when the disk angles are non-zero. Thus, disk motion in the X-Y plane may be controlled by tilting the disk. Similarly, translation in the X-Y plane changes the moments applied to the disk and therefore affects the disk angles. Thus, the lateral and rotational components are intrinsically coupled.

Consolidating (5) and the forces and moments, the disk equations of motion can be represented as first-order differential equations the form

$$\frac{d}{dt}\begin{bmatrix} q \\ \dot{q} \end{bmatrix} = \begin{bmatrix} \dot{q} \\ f(q, \dot{q}, w) \end{bmatrix} \tag{6}$$

where the kinematic variables are gathered in the vector $q = [x, y, z, \theta, \varphi]^T$, w is the vector of transformer variables defined in Section. 4.2, and $f(q, \dot{q}, w)$ is the vector function of the normalized forces and torques from (5).

4.2. Electrical subsystem equations

The transformer-capacitance modeling approach has been extensively described elsewhere and is only briefly reviewed. Figs. 3 and 5 show schematics to clarify how the transformers are connected to the electrodes in Figs. 2. Let w_k be the vector of currents and voltages associated with the electrode pair $\{\mathcal{E}_k, \mathcal{E}_{1k}\}$ and its corresponding transformer. Using the models from [11,12], the equations of motion are

$$\begin{aligned} M_k(q)\dot{w}_k &= A_k w_k \pm B_{1k} i_\mathrm{ct} + B_{2k} v_{\mathrm{c},k} \\ v_{\mathrm{s},k} &= J_k w_k \end{aligned} \quad k = 1, \ldots, 4 \tag{7}$$

for the primary electrode pairs, and

$$\begin{aligned} M_k(q)\dot{w}_k &= A_k w_k \pm 0.1 B_{1k} i_\mathrm{ct} \\ v_{\mathrm{s},k} &= J_k w_k \end{aligned} \quad k = 5, 6 \tag{8}$$

for the lateral electrodes. As discussed in [11], these equations are overdetermined but convenient to use when describing the transformers. The "mass matrices" $M_k(q)$ depend on the disk coordinates q because the disk position establishes the electrode–disk capacitances, however, the M_k are not full rank. Furthermore, the secondary voltages $v_{\mathrm{s},k}$ are states in the extended models and so their coupling to $v_{\mathrm{c},k}$ is not evident in these expressions. All matrices and vectors are compatibly dimensioned. The "±" associated with B_{1k} is a consequence of a single current source supplying the center tap currents to two transformers. For example, in Fig. 3 the current source, which is itself a transformer that is not shown for the sake of clarity, supplies current to electrode pairs $\{\mathcal{E}_1, \mathcal{E}_{11}\}$ and $\{\mathcal{E}_2, \mathcal{E}_{12}\}$. Thus, B_{11} would be assigned "+ ", whereas B_{12} would be assigned "−" due to the change in current polarity. The lateral electrode B_{1k} matrices have an additional 0.1 factor because the center tap current supplied to the lateral electrode transformers is one tenth that of the primary electrode transformers. Furthermore, the lateral electrode voltages are not regulated with a control signal so B_{2k}, $k = 5, 6$, are not present in (8). The transformer subsystems in (7) and (8) are consolidated into a single state-space representation

$$\begin{aligned} M(q)\dot{w} &= Aw + B_1 i_{\mathrm{ct}} + B_2 v_{\mathrm{c}} \\ v_{\mathrm{s}} &= Jw, \end{aligned} \tag{9}$$

where

$$\begin{aligned} M(q) &= \mathrm{diag}(M_1, M_2, M_3, M_4, M_5, M_6), \\ A &= \mathrm{diag}(A_1, A_2, A_3, A_4, A_5, A_6), \\ J &= \mathrm{diag}(J_1, J_2, J_3, J_4, J_5, J_6), \\ B_1 &= \begin{bmatrix} B_{11} \\ -B_{12} \\ B_{13} \\ -B_{14} \\ 0.1B_{15} \\ -0.1B_{16} \end{bmatrix}, \quad B_2 = \begin{bmatrix} B_{21} & 0 & 0 & 0 \\ 0 & B_{22} & 0 & 0 \\ 0 & 0 & B_{23} & 0 \\ 0 & 0 & 0 & B_{24} \\ 0 & 0 & 0 & 0 \\ 0 & 0 & 0 & 0 \end{bmatrix}, \end{aligned}$$

and where w and the vectors of amplitude-modulated control voltages and sense voltages are defined

$$w = \begin{bmatrix} w_1 \\ \vdots \\ w_6 \end{bmatrix}, \quad v_{\mathrm{c}} = \begin{bmatrix} v_{\mathrm{c},1} \\ \vdots \\ v_{\mathrm{c},4} \end{bmatrix}, \quad v_{\mathrm{s}} = \begin{bmatrix} v_{\mathrm{s},1} \\ \vdots \\ v_{\mathrm{s},6} \end{bmatrix}$$

The notation "diag" indicates a block-diagonal matrix (not necessarily square) whose diagonal blocks are given by the ordered matrices in the argument (the matrices may be scalar-valued, too). The "0" partitions in B_2 are appropriately dimensioned matrices of zero elements.

Additional states are contributed by the analog anti-alias filters and DAC smoothing filters shown in Fig. 4. The DAC smoothing filter transfer functions are denoted H_{sm}. The output of the smoothing filters are the signals $a_{\mathrm{c},k}$. The $v_{\mathrm{c},k}$ signals are created by sinusoidally modulating $a_{\mathrm{c},k}$,

$$v_{\mathrm{c},k} = a_{\mathrm{c},k}\cos(\omega_0 t + \phi_{u,k}), \; k = 1, \dots, 4 \tag{10}$$

where the phases are selected to achieve the maximum change in differential amplitude of the $\{\mathcal{E}_k, \mathcal{E}_{1k}\}$ electrode potentials. The smoothing filters are identical and are collectively modeled by the continuous-time state-space matrices $(A_{\mathrm{sm}}, B_{\mathrm{sm}}, C_{\mathrm{sm}}, 0)$ with state vector q_{sm}, input $a_{\mathrm{c}} = [a_{\mathrm{c},1}, a_{\mathrm{c},2}, a_{\mathrm{c},3}, a_{\mathrm{c},4}]^T$, and output v_{c}. The diagonal matrix of modulating sinusoids is defined,

$$\mathcal{D}_{\mathrm{c}} = \mathrm{diag}\left(\cos(\omega_0 t + \phi_{u,1}), \cos(\omega_0 t + \phi_{u,2}), \cos(\omega_0 t + \phi_{u,3}), \cos(\omega_0 t + \phi_{u,4})\right)$$

so $v_{\mathrm{c}} = \mathcal{D}_{\mathrm{c}} a_{\mathrm{c}}$.

Demodulating and filtering $v_{\mathrm{s},k}$ removes the $2\omega_0$ harmonic components. The filtering is accomplished using identical anti-alias filters whose transfer functions are denoted H_{aa}. The inputs to the anti-alias filters are

$$a_{\mathrm{s},k} = v_{\mathrm{s},k}\cos(\omega_0 t + \phi_{\mathrm{s},k}), \quad k = 1, \dots, 6, \tag{11}$$

The outputs of the anti-alias filters are the baseband signals ζ_k sampled by the DSP. The anti-alias filters are gathered into a single state-space representation $(A_{\mathrm{aa}}, B_{\mathrm{aa}}, C_{\mathrm{aa}}, 0)$ with state vector q_{aa}, input $a_s = [a_{\mathrm{s},1}, \dots, a_{\mathrm{s},6}]^T$, and output $\zeta = [\zeta_1, \dots, \zeta_6]^T$. The diagonal matrix of sinusoids that demodulate v_s is defined

$$\begin{aligned} \mathcal{D}_{\mathrm{s}} = \mathrm{diag}\big(&\cos(\omega_0 t + \phi_{s,1}), \cos(\omega_0 t + \phi_{s,2}), \cos(\omega_0 t + \phi_{s,3}), \\ &\cos(\omega_0 t + \phi_{s,4}), \cos(\omega_0 t + \phi_{s,5}), \cos(\omega_0 t + \phi_{s,6})\big) \end{aligned}$$

so $a_{\mathrm{s}} = \mathcal{D}_{\mathrm{s}} v_{\mathrm{s}}$. Collectively, the full coupled system is governed by

$$\begin{aligned} \dot{q}_{\mathrm{sm}} &= A_{\mathrm{sm}} q_{\mathrm{sm}} + B_{\mathrm{sm}} u_c \\ a_{\mathrm{c}} &= C_{\mathrm{sm}} q_{\mathrm{sm}} \\ M(q)\dot{w} &= Aw + B_1 i_{\mathrm{ct}} + B_2 \mathcal{D}_{\mathrm{c}} a_{\mathrm{c}} \\ v_{\mathrm{s}} &= Jw \\ \dot{q}_{\mathrm{aa}} &= A_{\mathrm{aa}} q_{\mathrm{aa}} + B_{\mathrm{aa}} \mathcal{D}_{\mathrm{s}} v_{\mathrm{s}} \\ \zeta &= C_{\mathrm{aa}} q_{\mathrm{aa}} \\ \frac{d}{dt}\begin{bmatrix} q \\ \dot{q} \end{bmatrix} &= \begin{bmatrix} \dot{q} \\ f(q, \dot{q}, w) \end{bmatrix}. \end{aligned} \tag{12}$$

4.3. Linearization

The governing equations are overdetermined and nonlinear, however, a periodic solution exists in which mean-value of the electrostatic forces and gravitational force sum to zero in the Z direction and exert zero net moment on the disk. Such a solution can be found when the disk's kinematic parameters are zero, i.e. $q = 0$, $\dot{q} = 0$. In this case, the capacitances associated with each electrode pair are equal, that is, $C_k = C_{1k}$, $k = 1, \dots, 6$. The center tap currents establish steady-state sinusoids for all the voltages and currents. The elements of u_{c} are adjusted such that mean value of the electrostatic forces balance the force due to gravity. The offset of u_c at this condition is denoted $\bar{u}$. The sinusoidal steady-state response of the transformer variables, denoted w_0, is computed from

$$M(0)\dot{w}_0 = Aw_0 + B_1 i_{\mathrm{ct}} - B_2 \mathcal{D}_c C_{\mathrm{sm}} A_{\mathrm{sm}}^{-1} B_{\mathrm{sm}} \bar{u}.$$

where $i_{\mathrm{ct}} = a_{\mathrm{ct}} \cos\omega_0 t$. The disk is considered at equilibrium because the mean values of the elements of $f(0, 0, w_0)$ are equal to zero. In this analysis the $2\omega_0$ components of the electrostatic forces are ignored because, as far as the kinematic variables are concerned, the disk acts like low pass filter. The steady-state solution of the anti-alias filter equations at equilibrium is denoted $\bar{q}_{\mathrm{aa}}$ and satisfies

$$\dot{\bar{q}}_{\mathrm{aa}} = A_{\mathrm{aa}} \bar{q}_{\mathrm{aa}} + B_{\mathrm{aa}} \mathcal{D}_{\mathrm{s}} J w_0.$$

The filter output $\zeta = C_{\mathrm{aa}} \bar{q}_{\mathrm{aa}}$ is essentially constant because the $2\omega_0$ terms are severely attenuated.

Linear variational equations can be determined by introducing perturbation variables relative to the steady-state values:

$$\begin{aligned} u_c &= \bar{u} + u, & q &= 0 + \delta_q, \\ q_{\mathrm{sm}} &= -A_{\mathrm{sm}}^{-1} B_{\mathrm{sm}} \bar{u} + \delta_{\mathrm{sm}}, & \dot{q} &= 0 + \delta_{\dot{q}}, \\ w &= w_0 + \delta_w, & q_{\mathrm{aa}} &= \bar{q}_{\mathrm{aa}} + \delta_{\mathrm{aa}}. \end{aligned} \tag{13}$$

The mass matrix, M, is continuously differentiable in a neighborhood of $q = 0$ and is represented (following elimination of higher order terms) as

$$\begin{aligned} M(q) = M(0) &+ \underbrace{\frac{\partial M}{\partial x}(0)}_{M_x}\delta_x + \underbrace{\frac{\partial M}{\partial y}(0)}_{M_y}\delta_y \\ &+ \underbrace{\frac{\partial M}{\partial z}(0)}_{M_z}\delta_z + \underbrace{\frac{\partial M}{\partial \theta}(0)}_{M_\theta}\delta_\theta + \underbrace{\frac{\partial M}{\partial \varphi}(0)}_{M_\varphi}\delta_\varphi \end{aligned} \tag{14}$$

where M_x, M_y, M_z, M_θ, and M_φ are defined as shown. Substituting (13) and (14) into (12) and retaining terms linear in the perturbation variables yields

$$\begin{aligned} \dot{\delta}_{\mathrm{sm}} &= A_{\mathrm{sm}} \delta_{\mathrm{sm}} + B_{\mathrm{sm}} u \\ M(0)\dot{\delta}_w &= A\delta_w + B_2 \mathcal{D}_{\mathrm{c}} C_{\mathrm{sm}} \delta_{\mathrm{sm}} \\ &\quad - \left(M_x\delta_x + M_y\delta_y + M_z\delta_z + M_\theta\delta_\theta + M_\varphi\delta_\varphi\right)\dot{w}_0 \\ \dot{\delta}_q &= \delta_{\dot{q}} \\ \dot{\delta}_{\dot{q}} &= \nabla_w f(0, 0, w_0)\delta_w + \nabla_q f(0, 0, w_0)\delta_q + \nabla_{\dot{q}} f(0, 0, w_0)\delta_{\dot{q}} \\ \dot{\delta}_{\mathrm{aa}} &= A_{\mathrm{aa}} \delta_{\mathrm{aa}} + B_{\mathrm{aa}} \mathcal{D}_{\mathrm{s}} J \delta_w \\ \zeta &= C_{\mathrm{aa}} \bar{q}_{\mathrm{aa}} + C_{\mathrm{aa}} \delta_{\mathrm{aa}} \end{aligned} \tag{15}$$

where $\nabla_w f(0,0,w_0)$, $\nabla_q f(0,0,w_0)$, $\nabla_{\dot q} f(0,0,w_0)$ are the gradients f with respect the variables w, q, and $\dot q$.

The mass matrix $M(0)$ is not full rank. The algebraic constraints are eliminated using the method discussed in [11]. The variable δ_1 represents the "essential" states associated with the transformer. The final time-periodic linear equations that describe the system in a neighborhood of the equilibrium solution are

$$\dot\delta_{\mathrm{sm}} = A_{\mathrm{sm}}\delta_{\mathrm{sm}} + B_{\mathrm{sm}}u \tag{16}$$

$$\dot\delta_1 = \Sigma_1^{-1}U_1^T\left(I - AW\right)\Big[AV_1\delta_1 + B_2\mathcal{D}_{\mathrm{c}}C_{\mathrm{sm}}\delta_{\mathrm{sm}} \tag{17}$$

$$- \left(M_x\delta_x + M_y\delta_y + M_z\delta_z + M_\theta\delta_\theta + M_\varphi\delta_\varphi\right)\dot w_0\Big] \tag{18}$$

$$\dot\delta_q = \delta_{\dot q} \tag{19}$$

$$\dot\delta_{\dot q} = \nabla_w f(0,0,w_0)\delta_w + \nabla_q f(0,0,w_0)\delta_q + \nabla_{\dot q} f(0,0,w_0)\delta_{\dot q} \tag{20}$$

$$\dot\delta_{\mathrm{aa}} = A_{\mathrm{aa}}\delta_{\mathrm{aa}} + B_{\mathrm{aa}}\mathcal{D}_{\mathrm{s}}J\delta_w \tag{21}$$

$$\zeta = C_{\mathrm{aa}}\bar q_{\mathrm{aa}} + C_a\delta_{\mathrm{aa}} \tag{22}$$

where U_1, V_1 and Σ_1 are defined from a singular value decomposition of $M(0)$,

$$M(0) = \begin{bmatrix} U_1 & U_2\end{bmatrix}\begin{bmatrix}\Sigma_1 & 0\\ 0 & 0\end{bmatrix}\begin{bmatrix}V_1^T\\ V_2^T\end{bmatrix},$$

and $W = V_2\left(U_2^TAV_2\right)^{-1}U_2^T$. It is necessary to express δ_w in terms of δ_1,

$$\begin{aligned}\delta_w &= (I - WA)V_1\delta_1 - WB_2\mathcal{D}_{\mathrm{c}}C_{\mathrm{sm}}\delta_{\mathrm{sm}}\\ &\quad + W\left(M_x\delta_x + M_y\delta_y + M_z\delta_z + M_\theta\delta_\theta + M_\varphi\delta_\varphi\right)\dot w_0.\end{aligned}$$

The states are merged to the compact representation

$$\begin{aligned}\dot\delta &= A_\delta(t)\delta + B_\delta(t)u\\ \zeta &= C_\delta\delta.\end{aligned}, \quad \text{where } \delta = \begin{bmatrix}\delta_{\mathrm{sm}}\\ \delta_1\\ \delta_q\\ \delta_{\dot q}\\ \delta_{\mathrm{aa}}\end{bmatrix}. \tag{23}$$

The offset in ζ has been dropped since it is removed in practice in any case. The equations are time-periodic with period $1/\omega_0$.

4.4. Analysis of the linearized model

The stability of (23) is analyzed using the disk and electrical subsystem parameters given in the Appendix and the following values for the carrier frequency, center tap currents, and control voltage offset to establish an equilibrium position for the disk: $\omega_0 = 2\pi\cdot 25\,\mathrm{krad/s}$, $a_{\mathrm{ct}} = 15.5\,\mathrm{mA}$, and each element of $\bar u$ is 1.77 V. The anti-alias filters and smoothing filters are 2-pole Butterworth with 1 kHz corner frequencies. This produces a system model with 66 states. An approximate time-invariant model can be derived by noting that the disk acts like a low-pass filter with regard to the electrostatic forces which rapidly vary at twice the carrier frequency, i.e. $2\omega_0$. Thus, the disk essentially responds to the mean value of the electrostatic forces so z, x, y, φ, and θ evolve on slow time scales compared to the currents and voltages associated with the electrical subsystem. Since the outputs of (23) are electrical analogs of the disk's kinematic variables (demonstrated below), and because there is additional band-limiting due to the smoothing and anti-alias filters, it is possible to derive an approximate discrete-time model of the system. First, consider the solution to an initial value problem for (23),

$$\delta(t) = \Theta(t,t_0)\delta(t_0) + \int_{t_0}^{t}\Theta(t,\tau)B_\delta(\tau)u(\tau)d\tau, \quad t \ge t_0, \tag{24}$$

where $\delta(t_0)$ is the initial condition represented in the perturbation variables, and $\Theta(t,t_0)$ represents the state transition matrix associated with (23). The "start time" t_0 determines the phase of the time-periodic steady-state solution about which the linearization is computed. It was shown in [11,12] that the choice of t_0 has no practical impact on the subsequent model, thus, it is assumed $t_0 = 0$ for the remainder of the analysis. For the experiments described in Section 6, the DSP implements the control laws with a sample period of $t_s = 1/5000$ second, i.e. the DSP sample rate is five times *slower* than ω_0. Successive samples at the DSP sample rate can be related using (24)

$$\begin{aligned}\delta((k+1)t_s) &= \Theta((k+1)t_s, kt_s)\delta(kt_s)\\ &\quad + \int_{kt_s}^{(k+1)t_s}\Theta((k+1)t_s,\tau)B_\delta(\tau)u(\tau)d\tau,\end{aligned} \tag{25}$$

where k is the integer sample index. Due to the periodicity of (23), the state transition matrix satisfies $\Theta(p/\omega_0, m/\omega_0) = \Theta^{p-m}(1/\omega_0,0)$ for any integers p,m so $\Theta((k+1)t_s,kt_s) = \Theta(t_s,0) = \Theta^5(1/\omega_0,0)$. An approximate time-invariant system is derived by assuming the control variable, u, is slowly varying over the time interval $\left[kt_s,(k+1)t_s\right]$, in other words, $u(\tau)$ is pulled out of the integral and replaced by $u[k]$ to yield

$$\begin{aligned}\delta[k+1] &= \Phi\delta[k] + \Gamma u[k]\\ \zeta[k] &= C_\delta\delta[k],\end{aligned} \tag{26}$$

where the notation $\delta[k]$ has replaced $\delta(kt_s)$ and

$$\Phi := \Theta(t_s,0), \quad \Gamma := \int_0^{t_s}\Theta(t_s,\tau)B_\delta(\tau)d\tau. \tag{27}$$

This analysis yields the four-input/six-output system denoted P. The frequency response of (26) is compared to empirical frequency response estimates in Section 6 and it is confirmed that the model accurately captures the disk dynamics. For sampling faster than the carrier, the method proposed in [12] can be used to generate similar approximate frequency responses.

5. Controller design

Numerical integration is used to compute Φ and Γ. The open-loop system has three eigenvalues outside the unit disk,

$$\{1.00128, 1.00140, 1.00140\}$$

with continuous-time approximations 6.4 and 7.0 rad/s. It will be shown that these eigenvalues can be associated with disk's vertical translation (the eigenvalue equal to 1.00128) and its two "tilt" degrees of freedom (the repeated eigenvalues equal to 1.00140 have geometric multiplicity two). This confirms that the disk dynamics evolve on a much slower time scale than the carrier frequency. There are also two pairs of stable lightly-damped eigenvalues that correspond two resonant modes with natural frequencies near 0.2 Hz. A neighborhood of these unstable eigenvalues are shown in Fig. 8.

The frequency response of P from the perspective of the input u_1 is shown in Fig. 9 (the various input–output channels are denoted ζ_1/u_1, etc.). Due to the symmetry of the disk and identical transformer models, a permutation of indices will produce the plant response to the other inputs, e.g., $\zeta_2/u_2 = \zeta_1/u_1$. Of particular interest is the presence of the feedthrough coupling in ζ_1/u_1 and the other "diagonal" channels. This coupling is caused by using each primary electrode for actuation and sensing. The coupling must be reduced to practically stabilize the disk. When manipulating the analytical model, this can be accomplished by "freezing" the disk dynamics and simply developing another model relating the input and output signals. In practice, a MIMO FIR filter is identified from measurements and is used as a feedforward filter (discussed in greater detail in Section 6). The coupling obscures the motional response of the disk — removing the feedthrough coupling reveals true dependence of the electrode–disk gap on the input as shown in Fig. 9.

A more convenient set of input–output variables is used for controlling the disk. The new input and output variables are defined $\{u_z, u_\varphi, u_\theta\}$ and $\{v_z, v_\varphi, v_\theta, v_x, v_y\}$, respectively, and are related to the

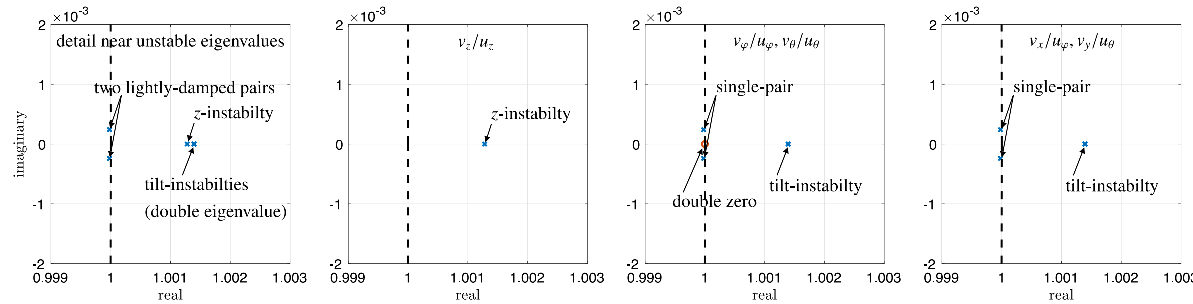

Fig. 8. Eigenvalues of Φ (far left) and detail of the unstable poles and zeros associated with the decoupled system transfer functions.

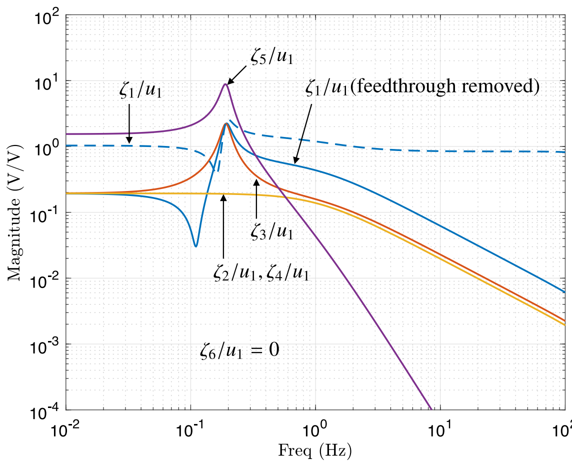

Fig. 9. Frequency response of P associated with input u_1. The ζ_1 output is shown with and without the feedthrough. The feedthrough in the ζ_k/u_l, $k \neq l$, channels is negligible as is the feedthrough in the lateral measurement (not shown here).

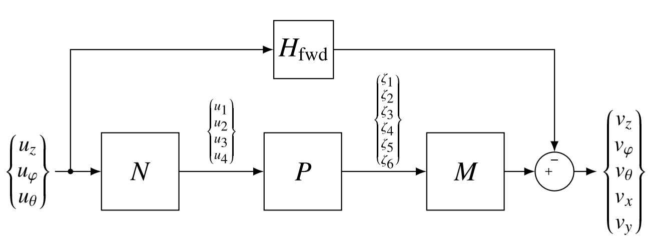

Fig. 10. The feedforward-compensated and decoupled plant $\tilde{P} = MPN - H_{\text{fwd}}$. The decoupling matrices are defined in Eqs. (29) and (28).

original input–output variables according to Fig. 10 where the matrices M and N are defined,

$$M = \begin{bmatrix} 0.5 & 0.5 & 0.5 & 0.5 & 0 & 0 \\ \frac{1}{\sqrt{2}} & 0 & -\frac{1}{\sqrt{2}} & 0 & 0 & 0 \\ 0 & -\frac{1}{\sqrt{2}} & 0 & \frac{1}{\sqrt{2}} & 0 & 0 \\ 0 & 0 & 0 & 0 & 1 & 0 \\ 0 & 0 & 0 & 0 & 0 & 1 \end{bmatrix} \tag{28}$$

and

$$N = \begin{bmatrix} 0.5 & \frac{1}{\sqrt{2}} & 0 \\ 0.5 & 0 & -\frac{1}{\sqrt{2}} \\ 0.5 & -\frac{1}{\sqrt{2}} & 0 \\ 0.5 & 0 & \frac{1}{\sqrt{2}} \end{bmatrix}. \tag{29}$$

These transformations can be explained as follows. After removing the feedthrough with the feedforward filter H_{fwd}, summing the compensated gap measurements and dividing by two yields the signal v_z. In other words, v_z can be interpreted as the average gap between the disk and electrodes. Similarly, since v_φ is basically the difference between ζ_1 and ζ_3, it represents an angle. From the input perspective, a moment is applied about the X coordinate axis, respectively, Y coordinate axis, when $u_\theta \neq 0$, respectively, $u_\varphi \neq 0$. A vertical electrostatic force is applied to the disk with v_z. With regard to compensating the feedthrough, the compensation can be performed using the original input–output variables, however, it is often more convenient to remove the feedthrough after the input–output transformations as illustrated in Fig. 10.

The system $\tilde{P} = MPN - H_{\text{fwd}}$ is used for controller design. It is referred to as the "decoupled" plant because its transfer function has the following form,

$$\tilde{P} = \begin{bmatrix} \star & 0 & 0 \\ 0 & \star & 0 \\ 0 & 0 & \star \\ 0 & \star & 0 \\ 0 & 0 & \star \end{bmatrix},$$

where the $\star$ entries are non-zero. Note that the $(1,1)$ element of $\tilde{P}$ is referred to as v_z/u_z, the $(2,2)$ element as v_φ/u_φ, and so forth. The frequency response magnitudes of the non-zero elements of $\tilde{P}$ are shown in Fig. 11. Also shown are the perturbation variables $\{\delta_z, \delta_\varphi, \delta_\theta, \delta_x, \delta_y\}$ associated with the disk's kinematic variables. The perturbation variables are not directly assessable in the physical system, however, they can be extracted from the model and compared to the electrical measurements $\{v_z, v_\varphi, v_\theta, v_x, v_z\}$. It is evident from Fig. 11 that the electrical measurements are excellent proxies for the disk's kinematic variables. This justifies the choice of subscript for the electrical measurements. The *scale factors* associated with the electrical measurements can be extracted from these graphs by comparing the magnitude of v_z/u_z to that of δ_z/u_z and so on. These estimated scale factors are given in Table 1.

Table 1
Scale factors (SF) from model.

	z (μm/V)	θ, φ (mrad/V)	x, y (mm/V)
SF	16.5	1.03	2.2

Classical loop-shaping design is applied to the decoupled plant in which SISO controllers, denoted G_z, G_φ and G_θ, are separately designed for v_z/u_z, v_φ/u_φ, and v_θ/u_θ. The closed-loop system block diagram is shown in Fig. 12. These controllers stabilize the closed-loop system. If the lateral measurements are available, it is possible to effectively regulate the lateral position of the disk, too. This is accomplished by feeding back the lateral position error to the *references* for the tilt degrees-of-freedom, denoted r_φ and r_θ. In other words, these references are driven by the output of the lateral controllers, G_x and G_y. Thus, the lateral position of the disk is controlled by tilting the disk.

The pole-zero locations of the entries of $\tilde{P}$ are shown in Fig. 8. The v_z/u_z transfer function has only one unstable pole at 1.00128 — the double eigenvalue at 1.00140 is canceled by a double zero at this location. Thus, this unstable eigenvalue is called the "z-instability" of

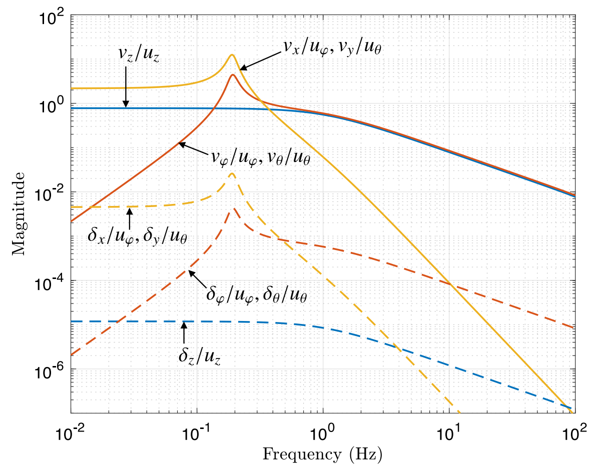

Fig. 11. Frequency response of $\tilde{P}$ compared to the frequency response of the disk's kinematic perturbation variables $\{\delta_z, \delta_\varphi, \delta_\theta, \delta_x, \delta_y\}$.

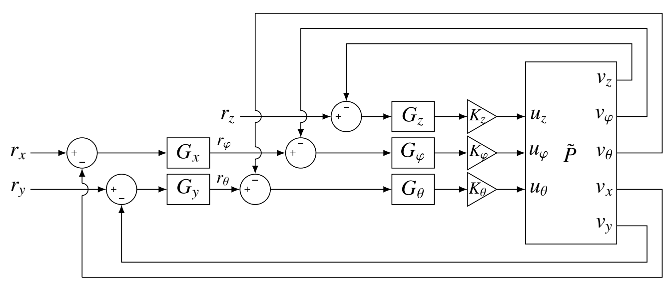

Fig. 12. Closed-loop block diagram.

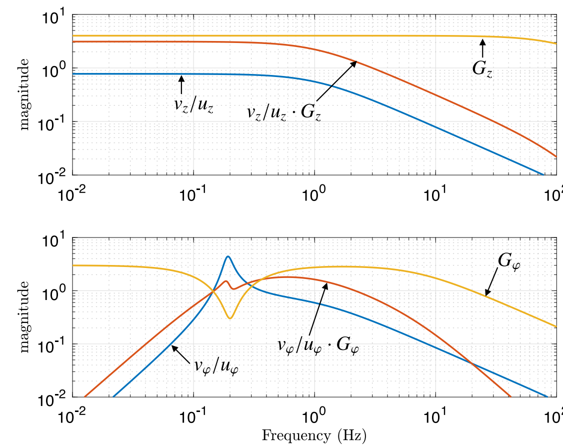

Fig. 13. Loop gains for v_z/u_z and v_φ/u_φ.

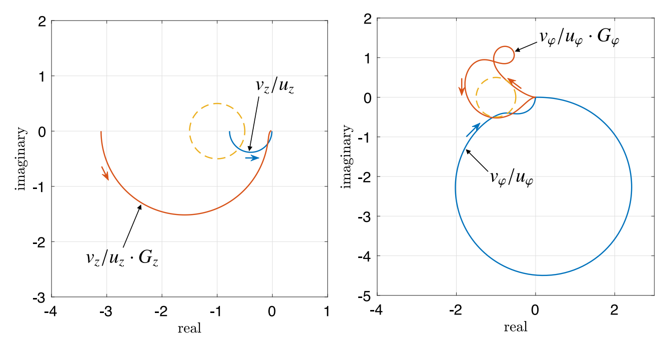

Fig. 14. Left: Nyquist plot of v_z/u_z and the loop gain illustrating one counterclockwise encirclement of -1 (only $\omega > 0$ shown). **Right:** Nyquist plot of v_φ/u_φ and the loop gain illustrating two counterclockwise encirclements of -1 (only $\omega > 0$ shown). The loop gain for v_θ/u_θ is identical to that of v_φ/u_φ. The arrows indicate the direction of increasing frequency.

the disk. The magnitude of v_z/u_z exhibits a low-pass characteristic whose corner frequency corresponds to this unstable pole. The lightly damped resonances are also missing because there is a double pair of zeros canceling the double pole pair slightly inside the unit disk. It is a simple matter to stabilize z-instability using constant gain feedback, however, due to uncertainty in the feedthrough cancellation at higher frequencies in the actual system, the controller gain is rolled off after 100 Hz. Thus, the (continuous-time) transfer function of the z-DOF controller, denoted G_z, is

$$G_z = 4\frac{200\pi}{s + 200\pi}. \tag{30}$$

The magnitude of the loop gain and controller frequency response are shown in Fig. 13 and the Nyquist plots are shown in Fig. 14.

Studying the tilt transfer functions reveals that v_φ/u_φ only has one unstable pole at 1.00140 — the other eigenvalue at this location is canceled by a single zero; the z-instability eigenvalue is also canceled. The unstable pole in v_φ/u_φ is referred to as a "tilt-instability". The resonance apparent in v_φ/u_φ near 0.2 Hz is due to the fact that only one pair of lightly-damped resonator poles is canceled in v_φ/u_φ. The same conclusion regarding the poles and zeros of v_θ/u_θ is reached. Thus, the tilt instabilities associated with the double eigenvalue 1.00140 are present in v_φ/u_φ and v_θ/u_θ, but only as a single unstable pole in each of these transfer functions. Other notable features of the tilt transfer functions are the double zeros at 1. This creates the ω^2 trend at low frequencies in Fig. 11 and implies that the disk angles must be zero at equilibrium in the stabilized system. This is sensible: there are no lateral forces acting on the disk other than those created by the electrostatic forces when the disk angles are non-zero (gravity is normal to the electrodes), thus, when the disk is at equilibrium, the angles must be zero.

Stabilizing the tilt-instability is an interesting problem because v_φ/u_φ (and, hence, v_θ/u_θ) is not *strongly stabilizable*. Although this can be illustrated by analyzing the parity interlacing property of the poles and zeros [15], analysis of the Nyquist plot is also insightful. The Nyquist plot of v_φ/u_φ is shown in Fig. 14. The fact that $|v_\varphi/u_\varphi| \to 0$ when $\omega \to 0, \infty$ implies that the loop gain must always have an even number of encirclements of $-1 + j0$. Since v_φ/u_φ has one unstable pole, G_φ must necessarily have an odd number of unstable pole(s) if stability is to be achieved. The following controller is implemented for v_φ/u_φ,

$$G_\varphi = \frac{14\pi}{s + 14\pi}\,\frac{s^2 + 0.2\omega_n s + \omega_n^2}{s^2 + 2\omega_n s + \omega_n^2}\,\frac{s+3}{s-3}, \quad \omega_n = 0.4\pi, \tag{31}$$

where the unstable pole is located at 3 rad/s. The loop gain magnitude is shown in Fig. 13 and the Nyquist plot is shown in Fig. 14. The controller notches the low-frequency resonance in v_φ/u_φ. An identical controller is used to stabilize the unstable pole in v_θ/u_θ associated with the second tilt-instability ($G_\theta = G_\varphi$).

Analysis of the plant model with the controllers (30) and (31) demonstrates that the closed-loop system is asymptotically stable — see the left eigenvalue plot in Fig. 15. The two pairs of lightly damped eigenvalues that correspond to the 0.2 Hz resonances are still present in the closed-loop system due to their cancellation by the G_φ and G_θ controllers. Regulation of the lateral position of the disk is also considered using measurements of the disk's lateral position. The transfer functions v_x/r_φ and v_y/r_θ are shown in Fig. 16 when the G_z, G_φ, and G_θ loops are closed, however, there is no feedback from the lateral measurements ($G_x = G_y = 0$). These frequency responses are associated with a stable system so the simple gains

$$G_x = 1, \quad G_y = -1, \tag{32}$$

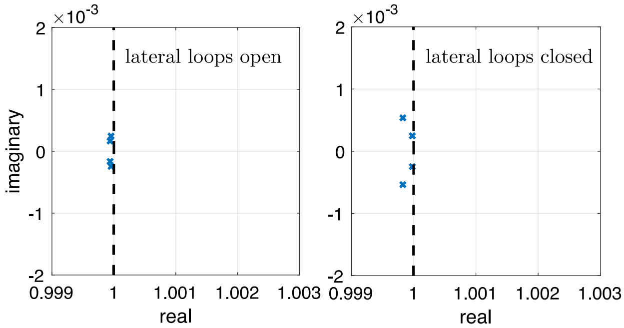

Fig. 15. Left: Eigenvalues with G_z, G_φ, and G_θ loops closed. **Right:** Eigenvalues after closing the G_x and G_y loops.

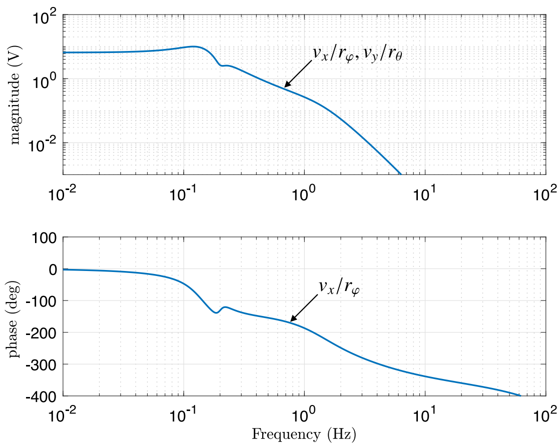

Fig. 16. Closed-loop frequency responses (from the model) of v_x/r_φ and v_y/r_θ when $G_x = G_y = 0$. Constant gains can be chosen for G_x and G_y in order to achieve regulation of v_x and v_y. The phase of v_y/u_θ is 180 degrees offset from the phase of v_x/r_φ.

are adequate for low-bandwidth regulation of x and y. The system eigenvalues are shown in Fig. 15.

6. Experimental results

6.1. Feedforward filter

The actuator-to-pick-off feedthrough must be reduced in order to stabilize the system. Although this configuration reduces the electrode voltages that are necessary for stabilizing the disk, it necessarily causes significant coupling from controller commands to measurements. The disk is not stabilizable in practice if the feedthrough is uncompensated. An accurate estimate of the feedthrough is required so instead of relying on the model to predict the feedthrough, it is simply measured when the disk is at rest on the bottom electrodes (the photoresist and/or small bumpers on the bottom glass plate ensure the disk does not come into contact with the electrodes). A typical empirical frequency response measurement is shown in Fig. 17 up to the sampling Nyquist frequency. These measurements were taken in the decoupled coordinates and represent the three-input/three-output feedthrough transfer function from $\{u_z, u_\varphi, u_\theta\}$ to the output of M in Fig. 11. There is no coupling to v_x and v_y so those elements in H_{fwd} are zero. The feedforward filter, H_{fwd}, that is used to cancel the feedthrough is simply an FIR fit to each scalar frequency response.

6.2. Closed-loop tests

The controllers are discretized and implemented as given in (30)–(32). Only minor adjustments to the gains $\{K_z, K_\varphi, K_\theta\}$ are performed.

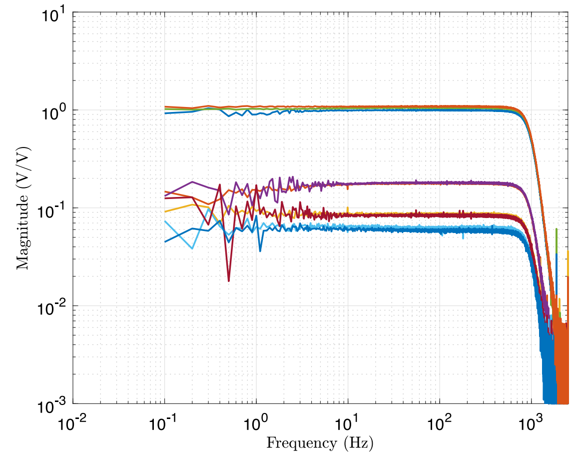

Fig. 17. Feedthrough estimates. The feedthrough associated with the v_z/u_z, v_φ/u_φ, and v_θ/u_θ channels have magnitude close to 1. The remaining six channels have magnitude close to 0.1. In general, all nine scalar feedthrough transfer functions must be reduced in magnitude by the feedforward filter H_{fwd}.

The disk is demonstrated to be stably suspended by introducing pulse disturbances into the closed-loop system at the input of $\tilde{P}$. The pulse is sequentially summed in with the controller outputs in order to perturb u_z, u_φ, and u_θ. The results of this experiment are shown in Fig. 18. The disk returns to its equilibrium position (0 V represents the equilibrium configuration of the disk because measurement offsets have been removed). The scale factors given in Table 1 can be used to convert the voltages into displacements and angles.

The input sensitivity function (S_i) frequency response is measured by injecting test signals at the input of $\tilde{P}$. The norm of S_i is shown as a function of frequency in Fig. 19. Although the closed-loop system is not particularly effective in rejecting disturbances at the plant input, the sensitivity function also shows that modest robustness to unstructured plant uncertainty is achieved. Regulation of the disk's lateral position is demonstrated in Fig. 20. Step references with 0.2 V amplitude are applied to r_x and r_y in separate experiments (this corresponds to lateral translational step values of approximately 0.44 mm).

6.3. Estimate of plant frequency response

An empirical frequency response of $\tilde{P}$ is derived from the measurement of two closed-loop frequency responses. Broadband and sinusoidal test signals are introduced at the plant input and yield the estimates of the closed-loop frequency response functions $\tilde{P}S_i$ and S_i. The open-loop plant frequency response is derived from these measurements on a frequency-by-frequency basis [16]. The physical plant exhibits coupling between input–output channels that is not present in the model. For example, v_φ and v_θ do not respond to signals applied to u_z in the decoupled plant model, however, the actual system shows u_z coupling to all outputs (Fig. 21). Nevertheless, v_z/u_z is the dominant transfer function associated with u_z. Similarly, the decoupled plant model indicates that only v_φ and v_x respond to u_φ, however, the estimates in Fig. 21 do show v_φ/u_φ and v_x/u_φ are dominant but that all outputs respond to u_φ. The same conclusion can be made concerning v_θ and v_y with respect to u_θ.

6.4. Discussion

The model compares quite favorably to the experimental estimates of the open-loop plant. The open-loop frequency response estimates confirm all features of the non-zero elements in the decoupled plant model: the low-pass characteristic of v_z/u_z; the rolling off of v_φ and v_θ as $\omega \to 0$; the relatively large low frequency gain of v_x/u_φ and v_y/u_θ; cf. Fig. 11 and Figs. 21. The physical plant exhibits cross-channel coupling

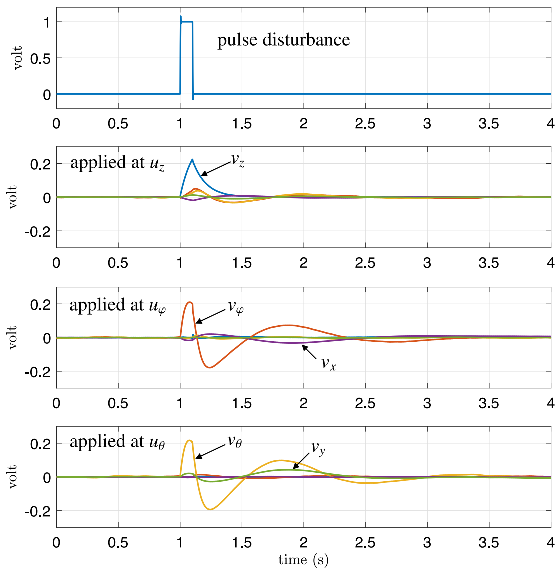

Fig. 18. Closed-loop experiments showing $\{v_z, v_\varphi, v_\theta, v_x, v_y\}$ in response to pulse disturbances applied at the input of $\tilde{P}$. This demonstrates closed-loop stability, i.e., the disk is suspended without contact.

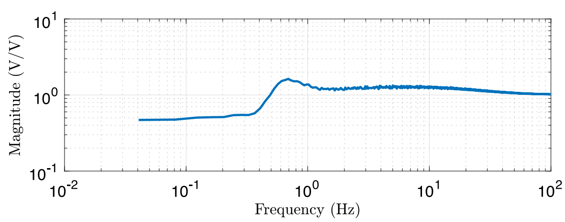

Fig. 19. Norm of input sensitivity function S_i.

that does not exist in the model, however, this is not surprising because small differences in the transduction gains associated with the primary electrode pairs and their transformers will destroy the symmetry in the model so that the decoupling transformations M and N actually mix all of the measurements related to the disks kinematic variables. The cross-channel coupling is especially evident in the lateral transfer functions v_x/u_φ and v_y/u_θ because the asymptotic magnitude of the measurements has an ω^{-1} trend as $\omega \to \infty$ whereas the model has an ω^{-3} trend.

Importantly, the model and experimental results support the thesis that the lateral degrees of freedom must be included in the analysis of the disk dynamics, regardless of whether additional lateral forces, such as fringe field effects, are present. In fact, inclusion of the lateral degrees of freedom fundamentally changes the disk model: the model developed in this paper demonstrates that it is not possible to hold the disk at an equilibrium position in which the disk is not normal to gravity (the model assumes the electrode planes are normal to gravity), thus, equilibrium values of φ and θ are always 0. Nevertheless, the lateral forces components created when the disk is not normal to gravity can be used to position the disk in the X-Y plane. The step response experiments also confirm that the disk angles return their equilibrium values as the lateral positions track step references.

The scale factors that have been estimated from the model (Table 1) have not been independently verified, however, vibrometer measurements of the beam system described in [11], which uses a transduction

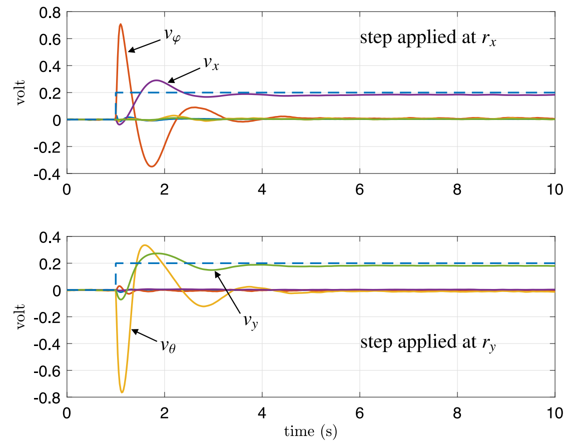

Fig. 20. Response of disk to lateral step reference signals of 0.2 V amplitude.

scheme that is identical to the present work, shows that the model-based scale factor deviates less than 10% from the measurement-based scale factor so similar accuracy is expected in this work.

7. Conclusion

Stabilization of an untethered and contact-free platform – a silicon disk – has been demonstrated. The disk is situated between pairs of electrodes that have been deposited on glass plates. The fringe-field forces exerted on the disk by the electrodes are negligible because the footprint of the primary electrodes is smaller than the disk diameter. Thus, the disk's lateral translational degrees-of-freedom are not constrained by fringe-field forces. An accurate disk model must include its lateral degrees-of-freedom and it was shown they are strongly coupled to the tilt degrees-of-freedom. Due to the lateral-tilt coupling, though, stabilizing the disk's tilt degrees-of-freedom also stabilizes its lateral degrees-of-freedom. The model, however, is not strongly stabilizable with only electrode–disk vertical gap measurements. In other words, the stabilizing controller is itself an unstable system. Outboard electrodes also provided direct measurements of the disk's lateral position. These measurements are used in an outer feedback loop to regulate the lateral position.

A potential application of the platform is in the study of micro-scale systems. The transduction scheme, based on measuring differential capacitances and exerting electrostatic forces using the same electrodes, scales reasonably well and it is envisioned that platforms 1 cm in diameter can be readily fabricated. Operating the disk *in vacuo*, however, will require adapting the controllers to the increased bandwidths associated with the vertical and tilt degrees-of-freedom. Furthermore, the low frequency lateral-tilt resonance will be essentially undamped. There are further control design issues to address with regard to what measurements are required in order for the system to be strongly stabilizable. These questions will be addressed in future papers.

CRediT authorship contribution statement

Michael Andonian: Conceptualization, Methodology, Software, Validation, Formal analysis, Investigation, Writing – original draft, Visualization. **Robert T. M'Closkey:** Conceptualization, Methodology, Writing – original draft, Writing – review & editing, Supervision, Project administration.

Declaration of competing interest

The authors declare that they have no known competing financial interests or personal relationships that could have appeared to influence the work reported in this paper.

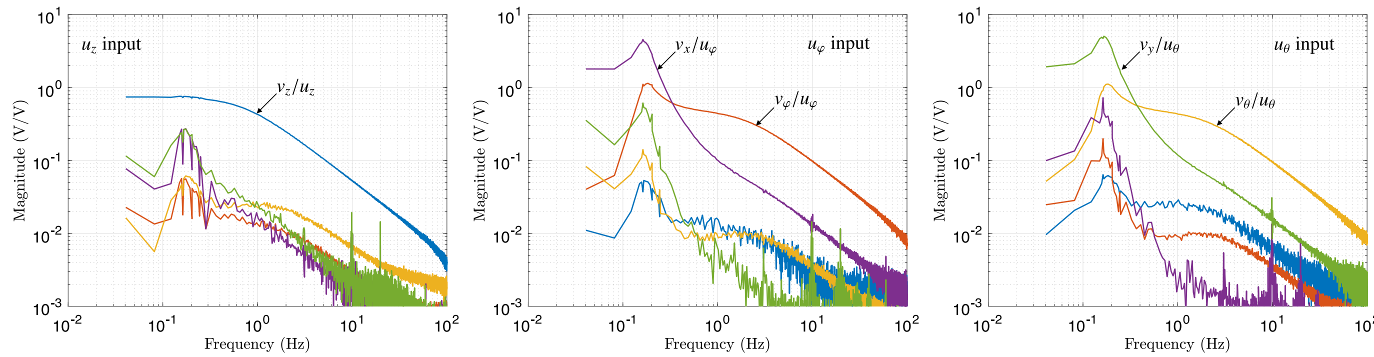

Fig. 21. Empirical frequency response estimates of $\tilde{P}$.

Acknowledgment

The authors thank the staff of the UCLA Nanoelectronics Research Facility. This research did not receive any specific grant from funding agencies in the public, commercial, or not-for-profit sectors.

Appendix. System parameters

Parameter	Value
Disk and electrode parameters	
disk radius	41 mm
disk thickness	400 μm
disk mass, m	4.92×10^{-3} kg
primary electrode area, A_p	10.3 cm^2
lateral electrode area	1.65 cm^2
electrode geometric center, r_0	22.2 mm
nominal electrode–disk gap, z_0	134 μm
in-plane moment of inertia, J_z	4.13×10^{-6} kg m^2
in-plane moment of inertia, J_{xy}	2.07×10^{-6} kg m^2
squeeze-film damping, c_z	3.3×10^4 s^{-1}
squeeze-film damping, c_θ, c_φ	1.79×10^4 s^{-1}
Transformer parameters	
primary inductance, L_1, L_2	2.1 H
secondary inductance, L_s	1.53 mH
leakage inductance, L_x	2.47 μH
mutual inductance, M_p	2.1 H
mutual inductance, M_s	57.6 mH
parasitic capacitance, C_p	17 pF
interwinding capacitance, C_i	70 pF
winding resistance (prim.), R_1, R_2)	504 Ω
winding resistance (sec.), R_{22}	0.54 Ω
shunt resistor on secondary, R_{21}	100 Ω
control resistor, R_c	100 Ω
electrode capacitances at equilibrium, C_k, C_{1k}	77.4 pF

References

[1] Atkinson JL. Electrostatic bearing. 1967, 3334949.
[2] Atkinson JL. Electrostatic bearing sensing and control circuitry. 1975, 3891285.
[3] Toda R, Takeda N, Murakoshi T, Nakamura S, Esashi M. Electrostatically levitated spherical 3-axis accelerometer, In: Proc. Fifteenth IEEE Intl. Conf. Microelectromech. Sys. 2002. p. 710–3.
[4] Han F, Gao Z, Li D, Wang Y. Nonlinear compensation of active electrostatic bearings supporting a spherical rotor. Sens. Actuator A Phys. 2005;119(1):177–86.
[5] Jin J, Higuchi T, Kanemoto M. Electrostatic levitator for hard disk media. IEEE Trans Ind Electron 1995;42(5):467–73.
[6] Jeon JU, Higuchi T. Electrostatic suspension of dielectrics. IEEE Trans Ind Electron 1998;45(6):938–46.
[7] van West E, Yamamoto A, Higuchi T. Manipulation of thin objects using levitation techniques, tilt control, and haptics. IEEE Trans. Automat. Sci. Eng. 2010;7(3):451–62.
[8] Kumar S, Cho D, Carr WN. Experimental study of electric suspension for microbearings. J. Microelectromech. Syst. 1992;1(1):23–30.
[9] Murakoshi T, Endo Y, Fukatsu K, Nakamura S, Esashi M. Electrostatically levitated ring-shaped rotational-gyro/accelerometer. Japan J Appl Phys 2003;42(4B):2468–72.
[10] Behbahani AH, Kim D, Stupar P, DeNatale J, M'Closkey RT. Tailored etch profiles for wafer-level frequency tuning of axisymmetric resonators. J. Microelectromech. Syst. 2017;26(2):333–43.
[11] Andonian M, M'Closkey RT. Sensing and control interface for precise gap control. Mechatronics 2018;56:277–86.
[12] Andonian M, M'Closkey RT. Identification and compensation of feedthrough in an unstable electrostatic bearing. Mechatronics 2020;65:102315.
[13] Seeger JI, Boser BE. Charge control of parallel-plate, electrostatic actuators and the tip-in instability. J. Microelectromech. Syst. 2003;12(5):656–71.
[14] Bao M, Yang H. Squeeze film air damping in MEMS. Sens. Actuator A Phys. 2007;136(1):3–27.
[15] Vidyasagar M. Control System Synthesis: A Factorization Approach. 3rd ed.. MIT Press; 1985.
[16] Wellstead PE. Non-parametric methods of system identification. Automatica 1981;17(1):55–69.

Michael Andonian received the B.S. degree and M.A. in mathematics from the University of Hawai'i at Manoa in 2010 and 2012, respectively, and the M.S degree in mechanical engineering from the University of California, Los Angeles, in 2018. He is currently pursuing the Ph.D. in mechanical engineering with a primary focus on control and identification of electromechanical systems. His present research is the development of a multi-degree of freedom electrostatic suspension system to test the dynamics of planar, micro-scale resonators.

Robert T. M'Closkey received the Ph.D. degree from the California Institute of Technology in 1995. He is currently a Professor in the Mechanical and Aerospace Engineering Department, University of California, Los Angeles. He develops micro-scale inertial sensors with a focus on Coriolis vibratory gyros (CVGs). His group has developed noise models, system identification approaches, and demonstrated wafer-scale trimming for CVGs built around axisymmetric resonators. He received the National Science Foundation CAREER Award for his research on MEMS inertial sensors and is a recipient of several teaching awards within the School of Engineering at UCLA.